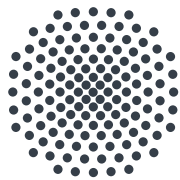


Spectroscopy of the $A\ ^2\Sigma^+$ to $H\ ^2\Sigma^+$, $H'\ ^2\Pi$ transition in nitric oxide.

Bachelor Thesis handed in to receive the degree “Bachelor of Science”
at the University of Stuttgart by Malte Kasten

12.10.2020

Examiner: Prof. Dr. Tilman Pfau
Co-Examiner: Dr. Harald Kübler



University of Stuttgart
5th Institute of Physics

Ehrenwörtliche Erklärung

Hiermit versichere ich gemäß §24.7 der Prüfungsordnung 2015,

1. dass ich die vorliegende Arbeit selbstständig verfasst habe,
2. dass ich keine anderen als die angegebenen Quellen benutzt und alle wörtlich oder sinngemäß aus anderen Werken übernommenen Aussagen als solche gekennzeichnet habe,
3. dass die eingereichte Arbeit weder vollständig noch in wesentlichen Teilen Gegenstand eines anderen Prüfungsverfahrens gewesen ist, und
4. dass das elektronische Exemplar mit den anderen Exemplaren übereinstimmt.

Stuttgart, den 12.10.2020

Malte Kasten

Zusammenfassung

Diese Bachelorarbeit wurde im Zusammenhang mit der Erforschung eines Stickstoffmonoxid Sensors auf Basis eines Laser getriebenen drei Level Schemas zur Anregung des Stickstoffmonoxids in hohe Rydbergzustände, in welchen das Stickstoffmonoxid durch Stöße ionisiert werden kann, verfasst. Der Fokus der Arbeit liegt auf der theoretischen Beschreibung des $H^2\Sigma^+$, $H'^2\Pi \leftarrow A^2\Sigma^+$ Übergangs, zusammen mit einer vollständigen Simulation dessen. Da die Energielevel des $H^2\Sigma^+$ und des $H'^2\Pi$ Zustands eine Distanz von etwa 10 cm^{-1} , sowie eine ähnliche Rotationskonstante $B \approx 2.0\text{ cm}^{-1}$ haben, muss die Störungstheorie in [1] verwendet werden, um das Koppeln des $H^2\Sigma^+$ an den $H'^2\Pi^+$ Zustand mit gleicher Parität zu erklären. Zusätzlich entstehen weitere lokale Störungen bei Überschneidung der Energieniveaus zwischen Zuständen gleicher Parität. Die Simulation wurde mithilfe von Daten aus [2] entwickelt und mit Daten aus [3] sowie eigenen Messwerten überprüft. Es wurde gezeigt, dass diese mindestens eine Übereinstimmung von 30 GHz aufweisen. Nachfolgend zu dieser Arbeit muss die Kontrolle der Messparameter, wie z.B. Laserleistung, Wellenlängen, etc., verbessert werden. Weiterhin müssen die Übergänge vermessen werden und in Hinsicht zu deren Übergangseffizienz untersucht werden.

Abstract

This thesis is written in conjunction with a nitric oxide trace gas sensor. The main focus of this thesis is on the $H^2\Sigma^+$, $H'^2\Pi \leftarrow A^2\Sigma^+$ transition, which is the second step in the three step transition scheme to high Rydberg states that can easily be brought into continuum via collisions. The interaction between the $H^2\Sigma^+$ and the $H'^2\Pi^+$ states and further local interactions have to be considered when simulating the above mentioned transition. A theoretical understanding of this transition is thus needed to build a simulation which reflects the experimentally shown transitions, and thus facilitates the search for the strongest transition on the path to bring molecules into continuum. The simulation is compared to data in [3] as well as to own measurement data. Furthermore the limits of the current measurement setup have been shown. Following up on this thesis, the measurement setup needs to be improved, such that measurement parameters of the apparatus are comparable between measurement runs and therefore the most efficient transition for Rydberg excitation can be found.

Contents

1	Motivation	1
2	Diatomic molecules	3
2.1	Degrees of freedom	3
2.2	Rotational states of a diatomic molecule	3
2.3	Electronic states of diatomic molecules	5
2.4	Splittings and coupling cases	6
2.4.1	Parity and Lambda splitting	6
2.4.2	Hund's cases	6
2.5	Selection rules for dipolar transitions and associated energies	8
2.5.1	Electronic transitions	8
2.5.2	Rotational transitions	8
2.5.3	Energies between states	9
2.6	Perturbation of close energy states	9
3	Experimental setup	11
3.1	Gas cell	11
3.2	UV laser system	11
3.3	Green laser system	12
3.4	Measuring routine	13
4	Simulation of the $H^2\Sigma^+, H'^2\Pi \leftarrow A$ transition	15
4.1	pgopher	15
4.2	Energy levels of ground state and first excited state of nitric oxide	15
4.2.1	$X^2\Pi$	15
4.2.2	$A^2\Sigma^+$	16
4.3	Finding correct interaction parameters between $H^2\Sigma^+, H'^2\Pi^+$	17
4.4	Comparison to experimental data from [3]	23
5	Experimental Results	25
5.1	R_{11} transitions	26
5.2	$H^2\Sigma^+ \leftarrow A^2\Sigma_{F_1}^+, J_A = 1.5$	28
5.3	Measurement stability	30
5.3.1	1080 nm long term frequency stability	30
5.3.2	Mode hops	31
5.3.3	Line strength	32
6	Summary and outlook	33
7	Appendix	37
7.1	Laser lock	37

1 Motivation

Nitric oxide is a key component in cardiovascular processes, since it is responsible for relaxation of arterial smooth muscles, as shown since 1980 in multiple publications, for example [4], [5] and [6]. Additionally nitric oxide has many other functions in the human body, like involvement in cellular signaling ([7]), signaling of diseases ([8]) and as mediator for defense responses ([9]). A first proof of principle of a sensor for nitric oxide in a buffer gas was shown in [10]. To accomplish the goal of a nitric oxide trace gas sensor, which requires < 1 l gas samples, the strongest transition lines have to be chosen to obtain the highest population in the high Rydberg state and therefore the highest sensitivity possible for sensing nitric oxide in a given gas sample. The transition scheme is shown in figure 1. Since the $A \leftarrow X$ has been thoroughly examined in [11], the next transition used for eventual Rydberg excitation of nitric oxide is $H \Sigma, H' \Pi \leftarrow A$, as shown in figure 1. A simulation is required in order to get a understanding of the perturbations present in the $H^2\Sigma^+, H'^2\Pi$ states as well as a guide for addressing predicted transitions. The simulation can later be confirmed by searching for features near predicted transitions in the electronic signal caused by double excitation by the $H^2\Sigma^+, H'^2\Pi \leftarrow A^2\Sigma^+$ laser into the continuum.

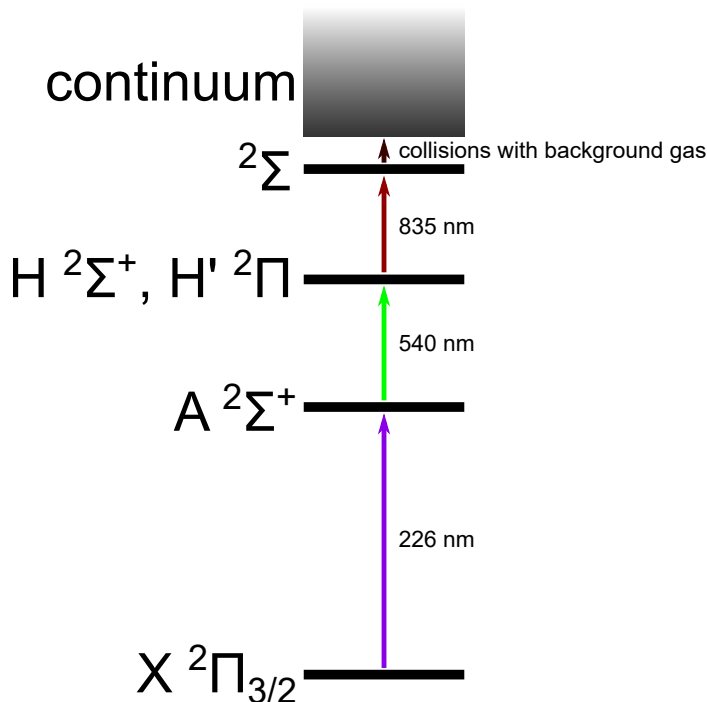


Figure 1: Transition schematic for a possible 3 level excitation of nitric oxide to Rydberg states. When the molecules reach continuum, the electron is ejected from the molecule and the charges can be detected when interacting with electrodes in the gas cell.

Motivation

The following chapter gives a brief overview over the relevant theory for this thesis. Chapter 3 describes the measurement setup used for all measurements done in conjunction with this thesis. Chapter 4 describes the development and theory behind the simulation of the $\text{H}^2\Sigma^+$, $\text{H}'^2\Pi$ states. Chapter 5 shows the results of the measurements done using the methods shown in chapter 3. Chapter 6 includes a summary of the content of this thesis as well as an outlook for the experiment.

2 Diatomic molecules

The following chapter gives an overview on the theory of diatomic molecules. The content of this chapter is based upon [12]. Some simplifications are made, since the resulting theory is accurate enough for the content of this thesis.

2.1 Degrees of freedom

Diatomic molecules are made up of two atoms bound together by their valence electrons whose wave functions cover the entire molecule. The symmetry leads to 6 degrees of freedom:

- 3 degrees of translation.
- 2 degrees of rotation. (1 around the intermolecular axis + 1 perpendicular to the intermolecular axis)
- 1 degree of vibration. (periodic change of internuclear distance)

The 3 degrees of translation can have continuous values of momentum assigned to them. These moments are Boltzmann distributed.

The potential 3 degrees of rotation are reduced to 2 degrees of rotation due to the rotational symmetry of the diatomic molecule around its intermolecular axis. All rotations can be described by a rotation around the intermolecular axis and one perpendicular to it, as long as a preferred direction can be identified.

In this thesis the vibrational states and their impact on the rotational state are disregarded since only transitions with a vibrational quantum number $v = 0$, so no vibration of the atoms, are considered.

2.2 Rotational states of a diatomic molecule

Since the bound electrons are very light compared to the atoms forming the molecule, $m_{\text{atom}} > 1800m_e$ where e denotes electrons, their contribution to the moment of inertia (see equation 2) of the molecule is negligible. Furthermore, for the sake of simplicity, the atoms can be treated as point particles. In the simplest case, the rigid rotator, depicted in figure 2a, one can assume the distance between the atoms to be a fixed length r , the mass of the two atoms given as m_1 and m_2 , rotating around the center of gravity. Following classical mechanics one can define the center of gravity of the molecule as the point, where $m_1 \cdot r_1 + m_2 \cdot r_2 = 0$. Since $r_1 - r_2 \stackrel{!}{=} r$ we can determine

$$\begin{Bmatrix} r_1 \\ r_2 \end{Bmatrix} = \frac{r}{m_1 + m_2} \cdot \begin{Bmatrix} m_2 \\ -m_1 \end{Bmatrix}. \quad (1)$$

The moment of inertia of the molecule perpendicular to the intermolecular axis is given by

$$I_{\perp} = m_1 \cdot r_1^2 + m_2 \cdot r_2^2 = \frac{m_1 m_2 \cdot (m_1 + m_2)}{(m_1 + m_2)^2} r^2 = \mu r^2 \quad (2)$$

with the reduced mass $\mu = m_1 m_2 / (m_1 + m_2)$. Following the assumptions above, the moment of inertia for rotations aligned with the intermolecular axis $I_{\parallel} = 0$ since $r_{1/2,\parallel} = 0$. Therefore the \perp subscript can be dropped, $I = I_{\perp}$, and all following equations regarding molecular rotation only include the rotation perpendicular to the intermolecular axis. The energy related to a given angular velocity ω is given by

$$E_{\text{rot}} = \frac{1}{2} I \omega^2 \quad (3)$$

with $\omega = 2\pi\nu$, where ν denotes the rotational frequency of the molecule. The angular momentum is given by $\mathbf{N} = I\omega$. Via substitution one gets $E_{\text{rot}} = \mathbf{N}^2 / (2I)$. This results in a rotational Hamiltonian $H_{\text{rot}} = E_{\text{rot}}$ for this system, since no potential contributes to the Hamiltonian. The energies for this quantum mechanical system are obtained by solving the time independent Schrödinger equation

$$H_{\text{rot}} \Psi_r = E_{\text{rot}} \Psi_r \quad (4)$$

with a rotational wave function Ψ_r . Since $\mathbf{N}^2 = \mathbf{r}^2 \times \mathbf{p}^2$ with the linear momentum $\mathbf{p}^2 = -\hbar^2 \Delta^2$, reduced Planck's constant \hbar and the Laplace operator $\Delta = d^2/dx^2 + d^2/dy^2 + d^2/dz^2$, one can rewrite (4) as

$$\Delta \Psi + \frac{2\mu}{\hbar^2} \cdot E_{\text{rot}} \Psi = 0. \quad (5)$$

The eigenvalues of (5) yield discrete energies

$$E_{\text{rot}} = \frac{\hbar^2 N(N+1)}{2I}. \quad (6)$$

with the rotational quantum number $N \in \mathbb{N}_0$. Hence the angular momentum $|\mathbf{N}|$ takes on eigenvalues of $\hbar\sqrt{N(N+1)}$.

In molecular physics most energies are given as wave numbers ($\bar{\nu} = \frac{E}{hc}$, unit: $[\text{cm}^{-1}]$) for easier use. The rotational term is given by

$$F(N) = BN(N+1) \quad (7)$$

with the rotational constant $B = \frac{\hbar}{4\pi I c}$, where c denotes the speed of light.

The model of a rigid rotator can be expanded to a non-rigid rotator, depicted in figure 2b, where the atoms are free to move under the influence of a harmonic potential with an equilibrium length r . The centrifugal force caused by the rotation of the molecule can now increase the distance between atoms to $r + \Delta r$. The new point of equilibrium is given, where the centrifugal force and the restoring force of the harmonic potential equalize. This slight increase in length changes the energy associated to the given rotational state. This perturbation can be shown to be very small already in the second order [12, p.103] and a quadratic correctional term with the centrifugal distortion constant D can be introduced, which results in

$$F(N) = BN(N+1) - DN^2(N+1)^2. \quad (8)$$

Introducing the electrons to the non-rigid rotator, the model changes to a symmetric top, depicted in figure 2c, where the angular momentum aligned to the intermolecular axis is given

by the electrons. Therefore the formerly introduced I_{\parallel} is no longer zero. The total angular momentum J of the molecule is then given by the sum of the angular momentum N of the nuclei and the angular momentum of the electrons composed of the orbital momentum and the spins. This perturbation results in an energy of

$$F(J) = B_v J(J+1) - D_v J^2(J+1)^2, \quad (9)$$

where v denotes the influence of the vibrations on the rotational constants. $B_v = B + \alpha(v+1/2)$ and $D_v = D + \beta(v+1/2)$, α and β are the vibrational factors influencing the rotational constant. Although this model is still highly simplified, it fits to the results obtained in experiments, see [2] or [3] for examples.

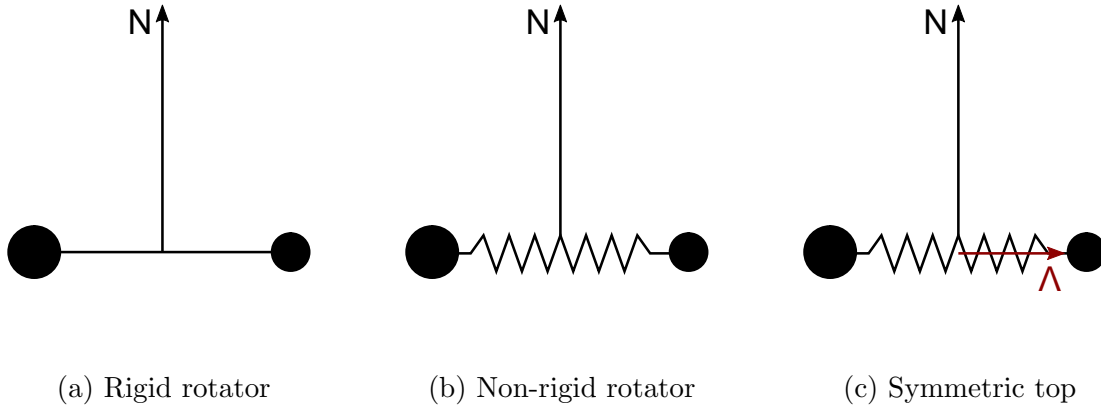


Figure 2: The figures show schematics of the rotational models introduced above. The harmonic potential of the non-rigid rotator is depicted as a spring between the nuclei. As written above, the angular momentum along the intermolecular axis, in the case of a symmetric top, is given by the total orbital momentum of the electrons projected on the intermolecular axis Λ .

2.3 Electronic states of diatomic molecules

To get the electronic states of the diatomic molecule and their corresponding angular momentum, the Schrödinger equation containing all interactions between the nuclei and the surrounding electrons

$$\frac{1}{m} \sum_{i \in e} \left(\frac{\partial \Psi}{\partial x_i} + \frac{\partial \Psi}{\partial y_i} + \frac{\partial \Psi}{\partial z_i} \right) + \sum_{j \in n} \frac{1}{M_k} \left(\frac{\partial \Psi}{\partial x_k} + \frac{\partial \Psi}{\partial y_k} + \frac{\partial \Psi}{\partial z_k} \right) + \frac{8\pi^2}{h^2} (E - V) \Psi = 0 \quad (10)$$

where i iterates over all electrons e with mass m and j iterates over both nuclei n with mass M_k , must be solved. Since an analytic solution can only be found in the case of a hydrogen atom, some assumptions need to be made in order to get an approximate solution for the given Schrödinger equation. First one assumes that the wave function can be split in two parts $\Psi = \Psi_e \cdot \Psi_n$ for electrons and nuclei respectively. It is shown by Born and Oppenheimer in [13], that

the first and second derivatives of the electronic eigenfunctions with variation of the internuclear distance are small enough, so they can be neglected. Thus the split Schrödinger equation can be further approximated. The wave function can be expressed in first approximation as

$$\Psi = \Psi_e \cdot \frac{1}{r} \cdot \Psi_n \cdot \Psi_r, \quad (11)$$

where r denotes the rotational wave function. Since the electrons are moving much faster than the nuclei due to their smaller mass, the motion of an oscillating molecule can be divided up in different temporal “snapshots” in its cycle, hence the distance dependent nuclear wave function can be transferred to a time dependent vibrational wave function, with the vibrational modes gained from the solution of the corresponding potential. It is evident from this, that for any given electronic eigenfunction there are multiple rotational and vibrational eigenfunctions that fulfill the approximated Schrödinger equation, describing the complex rovibrational structure of electronic states.

2.4 Splittings and coupling cases

2.4.1 Parity and Lambda splitting

As described in 2.3 the eigenfunction of a particular state can be approximated in first order as $\Psi = \Psi_e \cdot \frac{1}{r} \cdot \Psi_n \cdot \Psi_r$. In general it can be shown ([12, pp. 128-130]), that the rotator function can invert its sign upon spacial inversion, $\mathcal{P}\Psi_r = \Psi_r(-r) = \pm\Psi_r$ with the parity operator \mathcal{P} , depending on the angular momentum of the state. In general one can define the rotational parity of a given state as

$$\begin{aligned} e & : \mathcal{P}\Psi_r = +(-1)^{J^*} \Psi_r \\ f & : \mathcal{P}\Psi_r = -(-1)^{J^*} \Psi_r \end{aligned} \quad (12)$$

with

$$\begin{aligned} \text{number of electrons even} & : J^* = J \\ \text{number of electrons odd} & : J^* = J - \frac{1}{2} \end{aligned} \quad (13)$$

Since the spin of an electron is $\frac{1}{2}$, an even number of electrons always leads to a whole numbered total spin while an odd number of electrons leads to a half numbered spin. For any $\Lambda > 0$ the electronic function degenerates into two ($\Lambda = \pm|\Lambda|$) with a rotational e and f parity, which can result in a doublet splitting known as lambda doubling of any given rotational transition.

2.4.2 Hund’s cases

The five Hund’s cases (a-e, described in [12, pp. 219-226]) describe different coupling strengths between the angular momenta inside the molecule. Hund’s cases (a) and (b) are closer inspected since they are the cases present in the states investigated in this thesis.

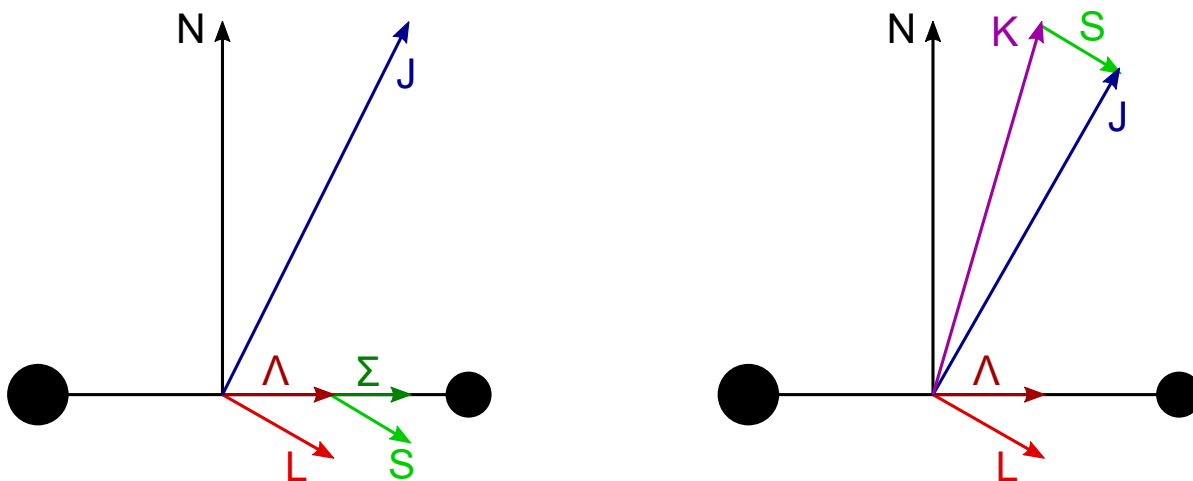
Hund’s case (a)

The coupling between L and S is strong, in terms of the molecular constants $A \gg B$, with spin-orbit constant A and rotational constant B . Both vectors can be combined and, due to

their precession around the intermolecular axis caused by an internal magnetic field between the nuclei, a combined quantum number $\Omega = \Lambda + \Sigma$ can be defined. $|\Lambda| \leq L$ is the total orbital momentum of the electrons projected on the intermolecular axis and $|\Sigma| \leq S$ is the total spin of the electrons projected on the intermolecular axis. As shown in the molecular orbital diagram in [14], $S = \frac{1}{2}$ and thus $\Omega = \Lambda \pm \frac{1}{2}$ resulting in two Ω for every given Λ with $J > \Omega$, as shown in figure 3a. $\Omega = \Lambda - \frac{1}{2}$ is denoted as electronic state F_1 , $\Omega = \Lambda + \frac{1}{2}$ is denoted as electronic state F_2 .

Hund's case (b)

The coupling between L and S is weak, in terms of the molecular constants $A \ll B$. The orbital momentum of the electrons still couples to the intermolecular axis and thus the quantum number Λ can be defined. Additionally $K = N + \Lambda$ can be defined. Now K and S together form $J = K + S$, as shown in figure 3b. $J = K + \frac{1}{2}$ is denoted as state F_1 and $J = K - \frac{1}{2}$ is denoted as state F_2 .



(a) Hund's case (a). The high frequency precession of L and S around the intermolecular axis due to the magnetic field between nuclei give rise to their projections Λ and Σ .

(b) Hund's case (b). The high frequency precession of L around the intermolecular axis due to the magnetic field between nuclei give rise to its projection Λ .

Figure 3: 3a shows the coupling of angular momenta within the molecule, which make up the total angular momentum J , for Hund's case (a), 3b shows it for Hund's case (b) respectively.

To every rovibrational state the sign, $+/-$, of the eigenfunction after reflection through an

Diatomic molecules

arbitrary plane containing the intermolecular axis can be assigned, with

$$+ : \begin{cases} F_1 \leftrightarrow e \\ F_2 \leftrightarrow f \end{cases} \quad (14)$$

$$- : \begin{cases} F_1 \leftrightarrow f \\ F_2 \leftrightarrow e \end{cases} \quad (15)$$

2.5 Selection rules for dipolar transitions and associated energies

2.5.1 Electronic transitions

As a first order approximation for high electron states, the eigenfunctions obtained by solving the Schrödinger equation of a hydrogen atom can be used. Since there is not only one nucleus in the molecule but two, the eigenfunctions are perturbed and thus selection rules $\Delta l = 0, \pm 1$ ¹ applying to the angular momentum quantum number l of the electron are softened considerably. This allows transitions between $s(l = 0)$ -like states and $d(l = 2)$ -like states with high pumping power.

For both Hund's cases (a) and (b) selection rules

$$\Delta \Lambda = 0, \pm 1, \Delta S = 0 \quad (16)$$

apply.

2.5.2 Rotational transitions

By calculating the electric dipole operator for transitions between different states using the wave functions obtained above by solving (5) the integrals do not vanish only for transitions²

$$\Delta J = J' - J'' = \begin{cases} -1 & \text{for all cases} & \text{(P-branch)} \\ 0 & \text{for at least 1 } \Lambda \neq 0 & \text{(Q-branch)} \\ +1 & \text{for all cases} & \text{(R-branch)} \end{cases} \quad (17)$$

Furthermore rotational parity selection rule can be defined

$$\Delta J = \pm 1 : \begin{cases} e \rightarrow e \\ f \rightarrow f \end{cases} \quad (18)$$

$$\Delta J = 0 : \begin{cases} e \rightarrow f \\ f \rightarrow e \end{cases} \quad (19)$$

¹ Δx describes the change in the quantum number x after a transition takes place.

² The quantum number belonging to the start state is marked with a $''$, while the end state is marked with a $'$. For a transition X_{ij} , i refers to the electronic " F " state of the end state, while j refers to the electronic " F " state of the start state.

2.5.3 Energies between states

The energy between the two electronic states is usually denoted as T_e . This energy is different from the energy of the rotational band origin since even a non vibrating molecule gets an energy offset given by the lowest state in the potential. The energy for the rotational band origin (for $v'' = 0$ and $v' = 0$) is usually written as T_{00} .

The energy difference between different rotational states is according to the selection rules introduced in 2.5.2 given by

$$F(J) = \left\{ \begin{array}{c} + \\ - \end{array} \right\} (2B_v J + 4D_v J^3) \left\{ \begin{array}{l} \text{for } J = J' = J'' + 1 \text{ (R-branch)} \\ \text{for } J = J'' = J' + 1 \text{ (P-branch)} \end{array} \right. . \quad (20)$$

In total the energy for any given state transition is

$$\bar{\nu} = T_{00} + F(J). \quad (21)$$

2.6 Perturbation of close energy states

As mentioned in 2.4.1 Σ states are non degenerate with a given parity, e or f . Π, Δ, \dots have a twofold degeneracy with opposing parity. For two energetically close lying electronic states with the same parity, the energies are perturbed (“pushed apart”) so that the resulting observed energies do no longer overlap.

In the case of the energetically close states $H^2\Sigma^+$, $H'^2\Pi$ with a band origin distance of $\sim 10 \text{ cm}^{-1}$, for $H^2\Sigma^+$ and $H'^2\Pi^+$, parities match up and result in a perturbation. Using energy levels obtained from experimental data in [2], a simulation of the unperturbed states is fitted in 4 accordingly to the theory presented in [1].

3 Experimental setup

The following section gives an overview over the gas cell and the electronic measurement setup. The second and third section give a closer look on the used laser systems. The fourth section explains the daily measuring routine.

3.1 Gas cell

The gas measuring setup is shown in figure 4. It consists of a glass cell with electrodes in a “house” configuration, for more detail on this see [15], with two flanges for gas input and output. The photo current produced by the Rydberg transition is very weak (\sim nA) and therefore must be amplified using the model 1211 transimpedance current preamplifier from DL instruments by a factor of $1 \frac{\text{V}}{\text{nA}}$. Depending on the current measurement setup, the amplifier can pick up a lot of noise, signal-to-noise ratio $\text{SNR} > 10$. When this happens the noise can be reduced by averaging over many laser frequency sweeps with an additional Fourier filtering using a frequency cut off of < 50 Hz, since most noise picked up by two thin long wires is caused by mains electricity at 50 Hz together with weaker components of higher frequency.

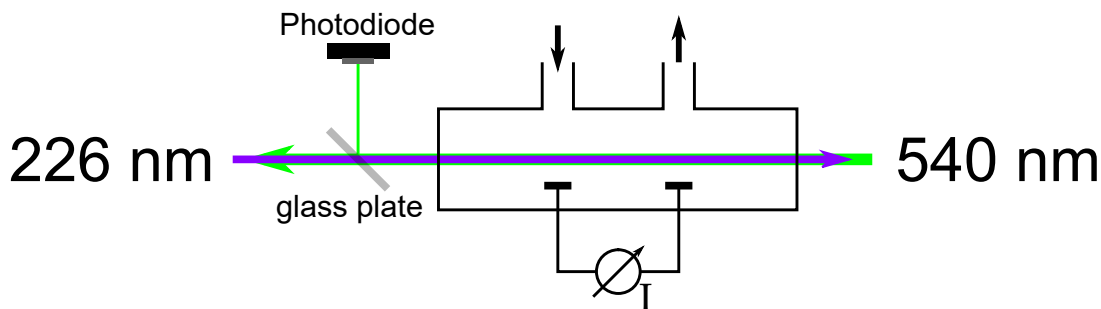


Figure 4: Experimental setup schematic. UV laser and green laser enter cell from opposite directions. Electrode setup is highly simplified in schematic, for more detail see [15]. The gas setup controlling the flow of pure nitric oxide at low pressure through the cell, including pressure gauge, ball valves, needle valves, etc., is not shown for simplicity. A UV translucent glass plate is used to reflect some of the 540 nm laser light on a photodiode for power monitoring. For more details on the laser systems see 3.2 and 3.3.

3.2 UV laser system

The laser system provided by M squared can be externally locked to a cavity to further increase frequency stability when stimulating a narrow molecular transition. The schematic of the UV setup can be found in figure 5. When the wavelength needs to be changed by more than 100 pm, the rotation of the doubler crystals needs to be optimized for the desired wavelength and the ring cavity must be optimized if necessary.

Experimental setup

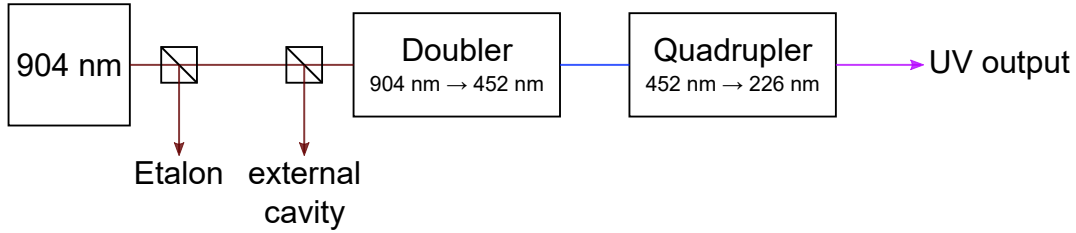


Figure 5: The UV laser system consist of a 532 nm pump laser which pumps a TiSa crystal inside a cavity which emits 904 nm laser light. The laser can be detuned. The wavelength chosen via a wavemeter can be locked via the Etalon lock with a width of ~ 50 MHz and held via an external cavity lock as shown in figure 20. Next the frequency is doubled and later quadrupled by non linear crystals within ring cavities.

3.3 Green laser system

The 540 nm laser system, which was setup in conjunction with [16], is shown in figure 6. It starts with a 1080 nm laser beam produced by a Toptica DL (Diode Laser) pro build in Littrow configuration, which is split off to a wavemeter and the external cavity before passing through a Keopsys CYFA fiber amplifier which increases the power up to 10 W. Next the laser is frequency doubled to 540 nm with a PPLN crystal. The output is then directed to the experiment. The wavelength of the laser can be changed via the grating in front of the laser diode for large steps above 100 pm, which the piezo for frequency scanning and fine tuning cannot cover.

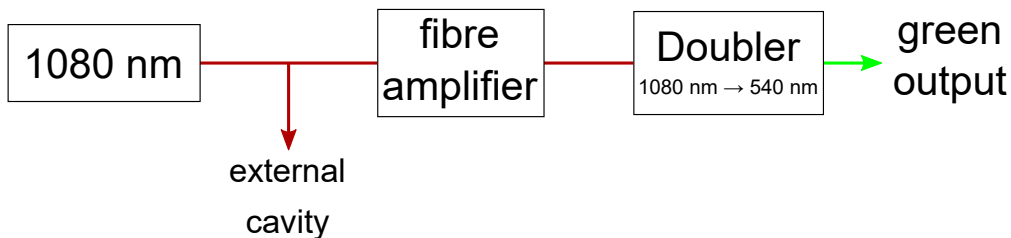


Figure 6: The green laser system consist of a 1080 nm laser diode. The laser can be detuned with a piezo or a screw on the grating. The wavelength chosen via a wavemeter is then stepped up to 10 W using a fibre amplifier and afterwards frequency doubled to 540 nm.

3.4 Measuring routine

The following routine was used to measure the experimental results shown in 5.

The gas pressure inside the apparatus is always held at low pressure < 10 mbar to prevent leakage from inside the system.

1. The gas pressure is lowered to 0.5 mbar. This ensures that the apparatus has as little oxygen and other gases in it, which can react with the nitric oxide.
2. The apparatus is flushed with nitric oxide at ~ 2 mbar for a few minutes, to reduce the contaminants in the apparatus which could interfere with the measurements requiring a pure nitric oxide atmosphere.
3. The nitric oxide bottle is closed and the nitric oxide supply line coming from the bottle is cut off. The pressure is lowered to the 0.7 mbar inside the gas cell required for the following measurements.
4. When the required pressure is reached, the ball valve leading to the pump is closed off and the apparatus is primed.
5. The UV laser is turned on. If a big change in wavelength is required, the change has to be done at least a few hours before the measurements are started to ensure that the doubler cavities are running stable after walking.
6. The etalon lock is set to the desired wavelength using the readout of a wavemeter. The resonator scan is turned on and the transmission signal of the UV laser through the gas cell is recorded.
7. The resulting dip in the transmission signal due to absorption by the gas is centered in the scan, which results in the maximum efficiency point reached, when turning off the scan.
8. The internal resonator scan is exchanged with the external PID controller scan and it is confirmed, that the dip is still centered in the scan.
9. The laser frequency is locked with the PID controller using the PDH signal produced by the cavity setup shown in figure 20 on the dip.
10. The green laser is turned on and set to the desired wavelength range using a wavemeter.
11. The power output of the UV as well as the green laser is measured using a power meter.
12. The electric signal produced by the ionized molecules is recorded and averaged as many times as is deemed necessary using a LeCroy WaveRunner 44MXi-A. Additionally a cavity signal produced by the fundamental of the green laser as well as the power drifts during sweeps are recorded.
13. Steps 10-12 are repeated as many times as necessary to measure as many transitions with desired parameters as needed.

Experimental setup

14. The gas setup is pumped out and all components containing nitric oxide are flushed with nitrogen.

4 Simulation of the $H^2\Sigma^+, H'^2\Pi \leftarrow A$ transition

This chapter describes the process of finding improved parameters, starting with constants given in [2], for the interaction between equal parity states in the H and H' states, which leads to a perturbation of the states. Data for this simulation was taken from [2]. Additionally [17] was used to confirm the rotational constants given in [2]. Furthermore data from [3] was used to evaluate the created simulation.

4.1 pgopher

The simulation program used to calculate the rovibrational transitions within the nitric oxide molecule is an open source program called “pgopher”. The input for the program is structured as a tree system, where structures have properties and can have substructures with further information about the transitions in question. For diatomic molecules the “LinearMolecule” structure can be used. It holds properties of the molecule, such as symmetry, and boundary values for the simulation, such as the range of rotational quantum numbers the simulation is performed for. The substructures available for this molecular model are the electronic states with their respective properties, such as band origins, rotational constants and other properties like spin-orbit coupling constants, and the transition moment describing the possible transitions between electronic states. Generally multi-level systems can be simulated. The simulation can approximate relative strength between branches as well as the intensity distribution within one branch taking into account that the occupation of rotational levels is Boltzmann distributed. The output can be provided via a graphical interface which can show an absorption line diagram and a Fortrat diagram or via the command line version as a list of all possible transitions with further information about the states involved in the transition. For more information on the software see [18].

4.2 Energy levels of ground state and first excited state of nitric oxide

The data given by [2] is for transitions between the ground state X and the states of interest H, H', while for the experiment the transition between A and H, H' is of interest. The properties of the H, H' states must first be obtained with the data from [2], such that the information of the interaction between H and H' can be transferred to the desired H, H' \leftarrow A transition. The ground state X and the first excited state A of nitric oxide are thus of importance in this thesis. The energy levels shown in the two subsections were created using constants taken from [19]. The constants have been confirmed in [11].

4.2.1 $X^2\Pi$

The ground level X of nitric oxide has an electronic state of

$$(\sigma 1s)^2(\sigma^* 1s)^2(\sigma 2s)^2(\sigma^* 2s)^2(\sigma 2p)^2(\pi 2p)^4\pi^* 2p.$$

Thus the only spin unpaired is in the valence shell, while all other electrons are bound in lower electronic states after Pauli's principle, which leads to a combination of all paired spins to 0. The total spin of the electrons is thus $S = \frac{1}{2}$ which results in a doublet state with multiplicity of 2. The orbital momentum of all electrons projected onto the intermolecular axis is expressed as the quantum number Λ . $\Lambda = 1$ results in a categorization as a Π state. Π states of Hund's case (a), which requires $A \gg B$, experience a splitting between the two possible orientations of the total angular momenta and the total spins projection on the intermolecular axis. Opposite orientation with $\Omega = \Lambda - \frac{1}{2} = \frac{1}{2}$ is denoted as F_1 . Parallel orientation with $\Omega = \Lambda + \frac{1}{2} = \frac{3}{2}$ is denoted as F_2 . The lowest possible total molecular angular momentum quantum number is given by $J = \Omega + N$ with the rotational quantum number $N = 0$. For F_2 and thus $\Omega = \frac{3}{2}$ there is no $J = \frac{1}{2}$ component, thus in figure 7a there are 11 states for F_1 but only 10 states for F_2 with $J < 11$. The splitting between states of same parity and same J but different F_i is given by the spin-orbit coupling constant which in this case is $A = 123.13582 \text{ cm}^{-1}$. The rotational constant of the ground state is given by $B = 1.69611 \text{ cm}^{-1}$, which fulfills the requirement for a Hund's case (a). The splitting between parities is of the order 0.01 cm^{-1} as seen in figure 7b.

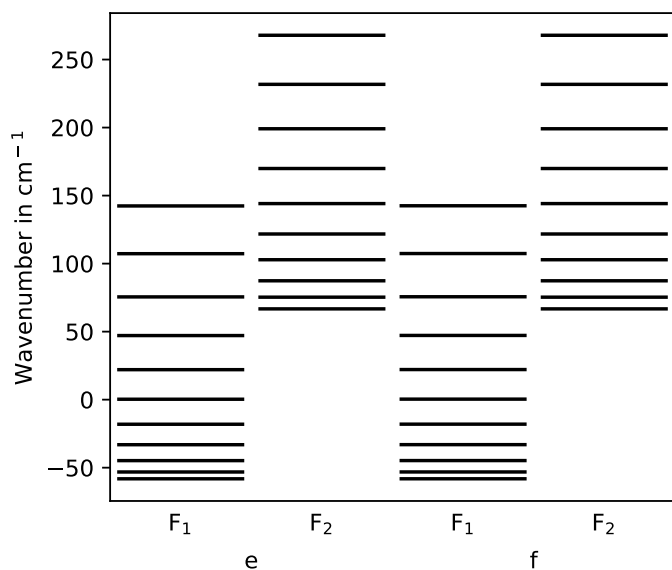
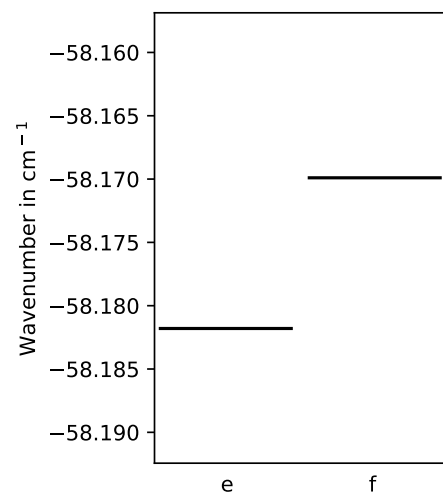
(a) Energy levels of $\text{X}^2\Pi$ with $J < 11$ (b) Energy levels of $\text{X}^2\Pi F_1$ with $J = 0.5$.

Figure 7: 7a shows splitting due to spin-orbit-coupling between F_1 and F_2 , 7b shows splitting between parities e and f for F_1 . Pgopher returns all energy levels in relation to the centroid of all states. This results in one band origin at $-A/2$ and the other at $A/2$.

4.2.2 $\text{A}^2\Sigma^+$

The first excited state A is populated by exciting the valence electron into the $3s\sigma$ -like orbital. Because the other electrons still combine due to Pauli's principle to a total spin of 0, the total spin of the molecule and thus the multiplicity is preserved. $\text{A}^2\Sigma^+$ is categorized as a Σ state,

since the state of the valence electron is classified by σ^*2p and thus the total orbital momentum of the electrons projected on the intermolecular axis $\Lambda = 0$, which results in only one parity. This electronic state can be classified as a Hund’s case (b), since the spin-orbit coupling is $A = 0 \text{ cm}^{-1}$, because $\Lambda = 0$ and thus no interaction potential between total electronic orbital momentum and total electronic spin is given. Because there is no preferred direction defined by the total electronic orbital momentum, the orientation of the spin has only a small influence on the state’s energy. The energetic position of the states is solely dependent on the rotational quantum number N . The total angular momentum of the molecule for the F_1 state is $J_1 = N + \frac{1}{2}$ and for the F_2 state is $J_2 = N - \frac{1}{2}$ with $J_1 = J_2 + 1$. Thus there is no J_2 for $N = 0$. As seen in figure 8a the energies of F_1 and F_2 with same N match up closely. A minor splitting between F_1 and F_2 for equal N arises due to the asymmetry, given by the spin rotation coupling constant γ , between the nuclei forming the molecule, which is shown in figure 8b.

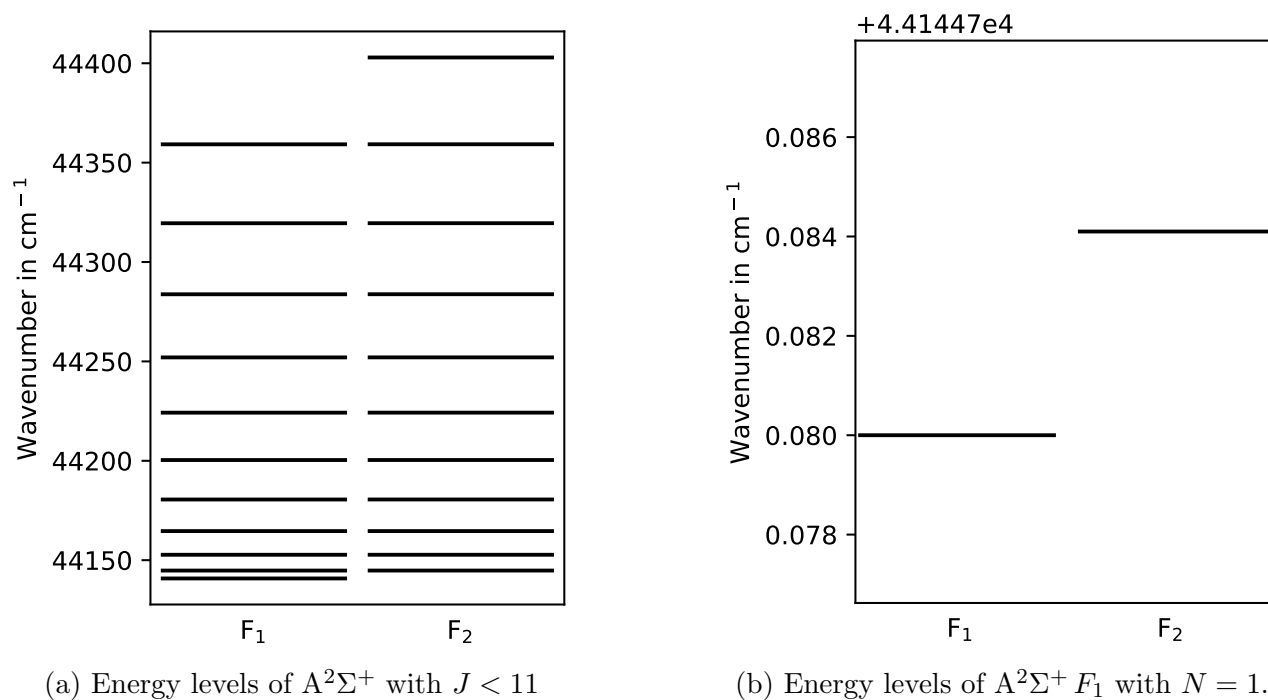


Figure 8: 8a shows splitting due to spin-orbit-coupling between F_1 and F_2 , 8b shows splitting between parities e and f for F_1 .

4.3 Finding correct interaction parameters between $\text{H}^2\Sigma^+, \text{H}'^2\Pi^+$

The rotational levels of the $\text{X}^2\Pi$ state as displayed in figure 7 in combination with the transitions from [2] starting at $\text{X}^2\Pi$ and ending either in the $\text{H}^2\Sigma^+$ or $\text{H}'^2\Pi$ state can be used to calculate the energy levels of $\text{H}^2\Sigma^+, \text{H}'^2\Pi$. For $+$ states, regarding a reflection through an arbitrary plane containing the intermolecular axis, parities match up to the electronic state, denoted by F_1 , according to equation 14, while “ $-$ ” states combine electronic state and parity according

Simulation of the $H^2\Sigma^+, H'^2\Pi \leftarrow A$ transition

to equation 15. Together with the selection rules from equations 18 and 19 this results in transitions with properties shown in table 1.

branch	$(H^2\Sigma, H'^2\Pi)^+ \leftarrow X^2\Pi$				$(H'^2\Pi)^- \leftarrow X^2\Pi$			
	$(H^2\Sigma, H'^2\Pi)^+$		$X^2\Pi$		$(H'^2\Pi)^-$		$X^2\Pi$	
	F	parity	F	parity	F	parity	F	parity
P_{11}	1	e	1	e	1	f	1	f
Q_{11}	1	e	1	f	1	f	1	e
R_{11}	1	e	1	e	1	f	1	f
P_{12}	1	e	2	e	1	f	2	f
Q_{12}	1	e	2	f	1	f	2	e
R_{12}	1	e	2	e	1	f	2	f
P_{21}	2	f	1	f	2	e	1	e
Q_{21}	2	f	1	e	2	e	1	f
R_{21}	2	f	1	f	2	e	1	e
P_{22}	2	f	2	f	2	e	2	e
Q_{22}	2	f	2	e	2	e	2	f
R_{22}	2	f	2	f	2	e	2	e

Table 1: This table gives an overview over all possible branches between $X^2\Pi$ and $H^2\Sigma^+, H'^2\Pi$. The transition rules are used to get the energy for $H^2\Sigma^+, H'^2\Pi$ from the transitional data in [2].

A corresponding energy sub-level in the ground state for a given transition to the excited state $(H^2\Sigma^+, H'^2\Pi)$ can be found using table 1. For a given transition in [2], the energy of the corresponding $X^2\Pi$ state from the pgopher simulation can be found. Thus the energy of the corresponding excited state

$$T_{H/H'} = T_X + \Delta T_{\text{transition}} \quad (22)$$

can be calculated.

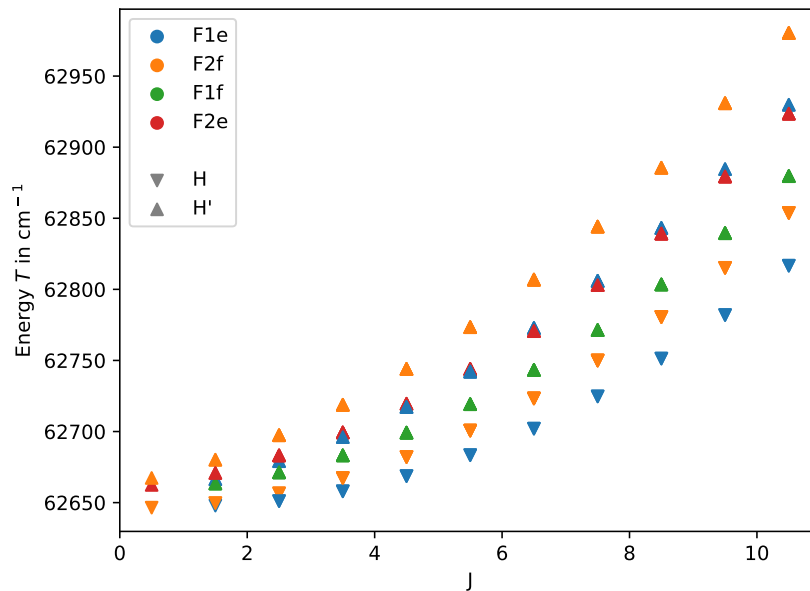


Figure 9: Energy levels of the excited $\text{H } ^2\Sigma^+, \text{H}' ^2\Pi$ gained by using transitional energies from [2] calculated with equation 22 and table 1.

For the following steps it needs to be assumed, that there is no systematic error in the measurement done in [2], which is supported by the comparison of the transitional energies for a $\text{H } ^2\Sigma^+, \text{H}' ^2\Pi \leftarrow \text{A } ^2\Sigma^+$ transition, calculated from the energy levels found in the following, to transitional data given in [3]. A general error in the measurement data is still possible, since the evaluated photographic plates were captured by an other group and thus the group working on [2] had no influence on the accuracy of the data they received. The energies of the excited states are shown in figure 9. To extrapolate the energy levels of the $\text{H } ^2\Sigma^+, \text{H}' ^2\Pi$ states for arbitrary J , a theoretical model of the observed energies is required.

According to 2.2 simple unperturbed states have the rotational energy

$$F(J) = B_e \cdot J(J+1) + D_e \cdot J^2(J+1)^2 + \begin{cases} -\frac{A}{2} & \text{for } F_1 \\ \frac{A}{2} & \text{for } F_2 \end{cases} \quad (23)$$

depending on the total angular momentum of the molecule J .

According to [1], further terms of interaction between two different electronic states with the same total molecular angular momentum have to be added, when the energy gap is sufficiently small. In figure 9 it is clearly visible, that the $\text{H } ^2\Sigma^+$ state is lower than the $\text{H}' ^2\Pi$ state for $J = 0.5$, the distance is found to be $C \approx 10 \text{ cm}^{-1}$. For equal parity (both positive or both negative) this results in an interaction. $\text{H } ^2\Sigma^+$ and $\text{H}' ^2\Pi^+$ fulfill this requirement stated by [1], which results in a first order linear splitting in equal J , while the energy contributions by rotational constants is of quadratic and higher order. A perturbation for large J between two different electronic states is still present, since the rotational constants of the two excited states

Simulation of the $\text{H } ^2\Sigma^+, \text{H}' ^2\Pi \leftarrow \text{A}$ transition

are similar and thus the gap between unperturbed states remains of almost constant width. The close match of rotational constants will later be shown to be true for $\text{H } ^2\Sigma^+$ and $\text{H}' ^2\Pi$.

As [2] states, the rotational energies without perturbation of the excited states are calculated by using rotational constants B_v , D_v and spin-orbit-coupling constant A listed in table 2.

	$\text{H } ^2\Sigma^+$	$\text{H}' ^2\Pi$	Source
Origin	62646.75	62658.55	[2], corrected by centroid of $\text{X } ^2\Pi$ states
A	0	1.442	[17]
B	1.994	2.006	[2]
D	$6 \cdot 10^{-6}$	$6.18 \cdot 10^{-6}$	[17]

Table 2: Molecular constants used in pgopher simulation

The difference between the theoretical unperturbed states and the energies shown in figure 9 is depicted in figure 10. For both excited states of $+$ parity a clear linear J dependence of the energy difference can be found. It is important to note that the energy difference behaves anti symmetrically for both excited states with equal alignment of electronic spin to electronic orbital momentum. This suggests an interaction between $\text{H } ^2\Sigma^+$ and $\text{H}' ^2\Pi^+$.

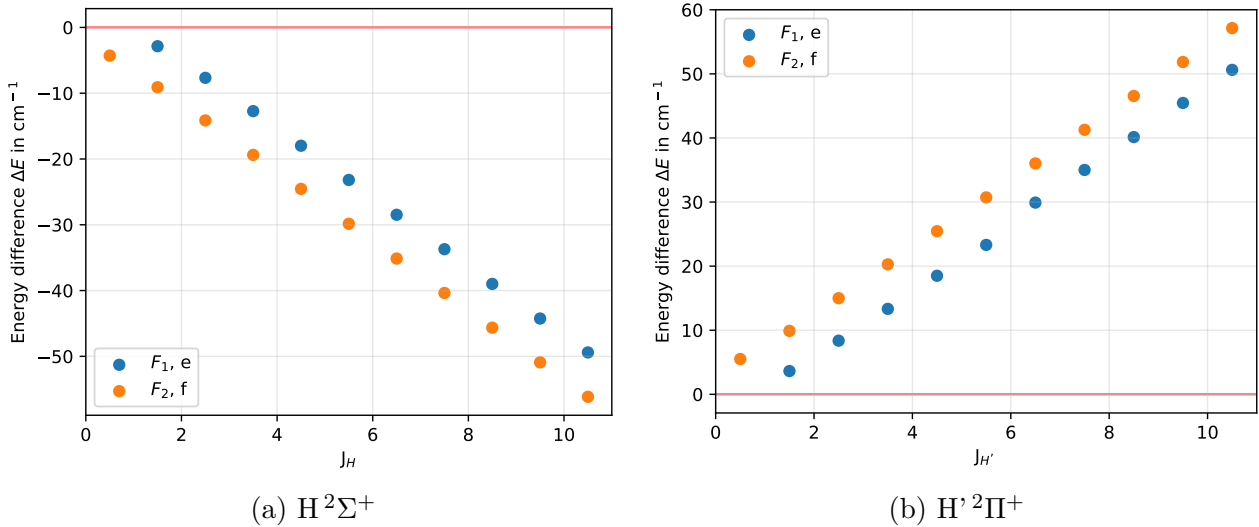


Figure 10: Energy difference between energy levels obtained via equation 22 with transitional data from table 2 in [2] and the simulated energy levels $T_{\text{exp}} - T_{\text{sim, unpert}}$ using the rotational constants from table 4 in [2].

The energetically lower state $\text{H } ^2\Sigma^+$ is “pushed” down in energy, while the energetically higher state $\text{H}' ^2\Pi^+$ is “pushed” up, which decreases the interaction between the states for increasing J . According to [1] a J_0 can be defined, at which the two energy lines will intersect. In the given case the energy lines do not cross, thus $J_0 < 0$. The distance between the energies for $J = 0$ and no spin-orbit coupling is $C \approx 10 \text{ cm}^{-1}$. The slope derived from figure 10 is $V \approx \pm 5.5 \text{ cm}^{-1}$. A theoretical crossing between energies can be calculated to be around $J_0 \approx -1.5$. For $J \approx J_0$,

[1] states, that the perturbation gets larger and requires a correction term. For small differences in the rotational constants B this correction of the linear perturbation is similar to an avoided crossing of the form

$$\Delta E_{\text{pert}}(J) = \text{sgn}(J - J_0) \cdot S \sqrt{V^2 \cdot N(N+1) + \left(\frac{C}{2}\right)^2} + \frac{C}{2} \quad (24)$$

$$= S \sqrt{V^2 \cdot N(N+1) + \left(\frac{C}{2}\right)^2} + \frac{C}{2} \quad (25)$$

with

$$J = N + \Lambda + \begin{cases} \frac{1}{2} & \text{for } F_1 \\ -\frac{1}{2} & \text{for } F_2 \end{cases}, \quad (26)$$

the sign S , interaction parameter³ V and the splitting at $J = 0$ between the different states C . Additionally there is a coupling between the $\text{H}'^2\Pi^+ F_1$ and $\text{H}'^2\Pi^- F_2$ states with rotational parities e , when they are intersecting at $J_0 = 6$ due to the perturbation between $\text{H}^2\Sigma^+$ and $\text{H}'^2\Pi^+$. With $J_0 > 0$, there is an interaction of the form

$$\Delta E_{\text{small pert}}(J) = S \cdot \text{sgn}(J - J_0) \cdot \sqrt{W^2(J - J_0)(J - J_0 + 1) + \left(\frac{F}{2}\right)^2} + \frac{F}{2}, \quad (27)$$

with the interaction parameter W and splitting at J_0 between states F . For the generally unperturbed $\text{H}'^2\Pi^-$ state a small linear dependency of the form

$$\Delta E_{\text{line}} = M \cdot J \quad (28)$$

is fitted to the data. To compensate for any offsets, an additional parameter U was introduced and optimized.

³ called α in [2], table 3

Simulation of the $\text{H } ^2\Sigma^+, \text{H}' ^2\Pi \leftarrow \text{A}$ transition

		S	V	C	W	F	M	U
$\text{H } ^2\Sigma^+$	F_1	-	5.282	9.824	-	-	-	1.238
	F_2	-	5.298	10.489	-	-	-	-0.347
$\text{H}' ^2\Pi^+$	F_1	+	4.908	6.205	0.326	1.703	-	-1.901
	F_2	+	5.260	7.215	-	-	-	-1.884
$\text{H}' ^2\Pi^-$	F_1	-	-	-	-	-	-0.006	0.521
	F_2	-	-	-	0.270	1.603	0.297	-1.938
[2]		-	5.43	11.8	-	-	-	-

Table 3: Fit parameters found for $\text{H } ^2\Sigma^+$ and $\text{H}' ^2\Pi$ for equations 24-28. All variables are given in cm^{-1} . The constants given in [2] are similar. Since [2] was written in 1963, the constants given above are improved constants gained by fitting to the data with a digital optimizer instead of fitting manually. To get more accurate parameters, more precise measurements need to be made.

Using the fit parameters obtained from a fit using equations 24-28 between unperturbed energy levels and energy levels shown in figure 9 are listed in table 3. The difference between the energies of $\text{H } ^2\Sigma^+$ and $\text{H}' ^2\Pi$ calculated from the data in [2] and the perturbed, with fit parameters from table 3, simulated data is shown in figure 11. A plot of the simulated energy levels overlapped with the energy levels in figure 9 is not shown, since the scale is too large to see the difference between the two energy level sets.

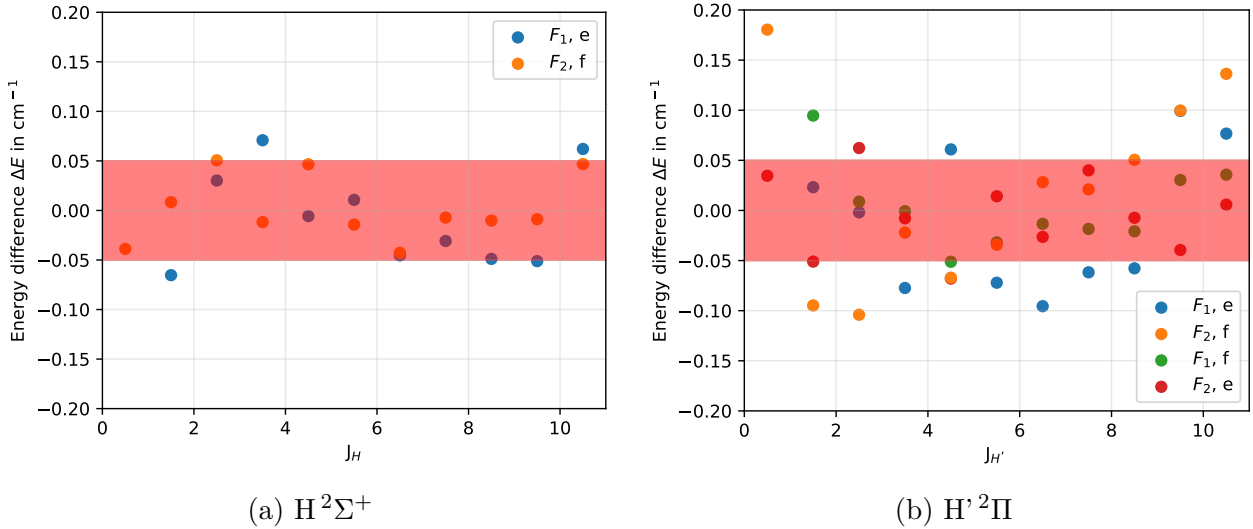


Figure 11: Energy difference between energy levels obtained via equation 22 with transitional data from table 2 in [2] and the perturbed simulated energy levels. The red shaded area is the maximum accuracy of $\pm 0.05 \text{ cm}^{-1}$ limited by the measurement technique in [2].

4.4 Comparison to experimental data from [3]

For $A^2\Sigma^+$ only the transition rules from table 1 for F_i and rotational parities following 14 are possible. The resulting transitions can be plotted in a Fortrat diagram. The line intensities are unknown. Overlaying all transitions with $A^2\Sigma^+, F_1$, since the $A^2\Sigma^+ \leftarrow X^2\Pi$ transition is driven via the P_{12} branch, on top of figure 2 from [3] with $F_A = 1$, since the lower transition $A^2\Sigma^+ \leftarrow X^2\Pi$ is driven via a P_{12} transition, a close match of the measured data to the simulation can be found as seen in figure 12. This makes a systematic error in the data in [2] very unlikely, since the systematic errors would need to be almost identical. This is further supported by the data shown in figure 15. When more transition are accurately measured, the simulation can be further checked and, if needed, improved.

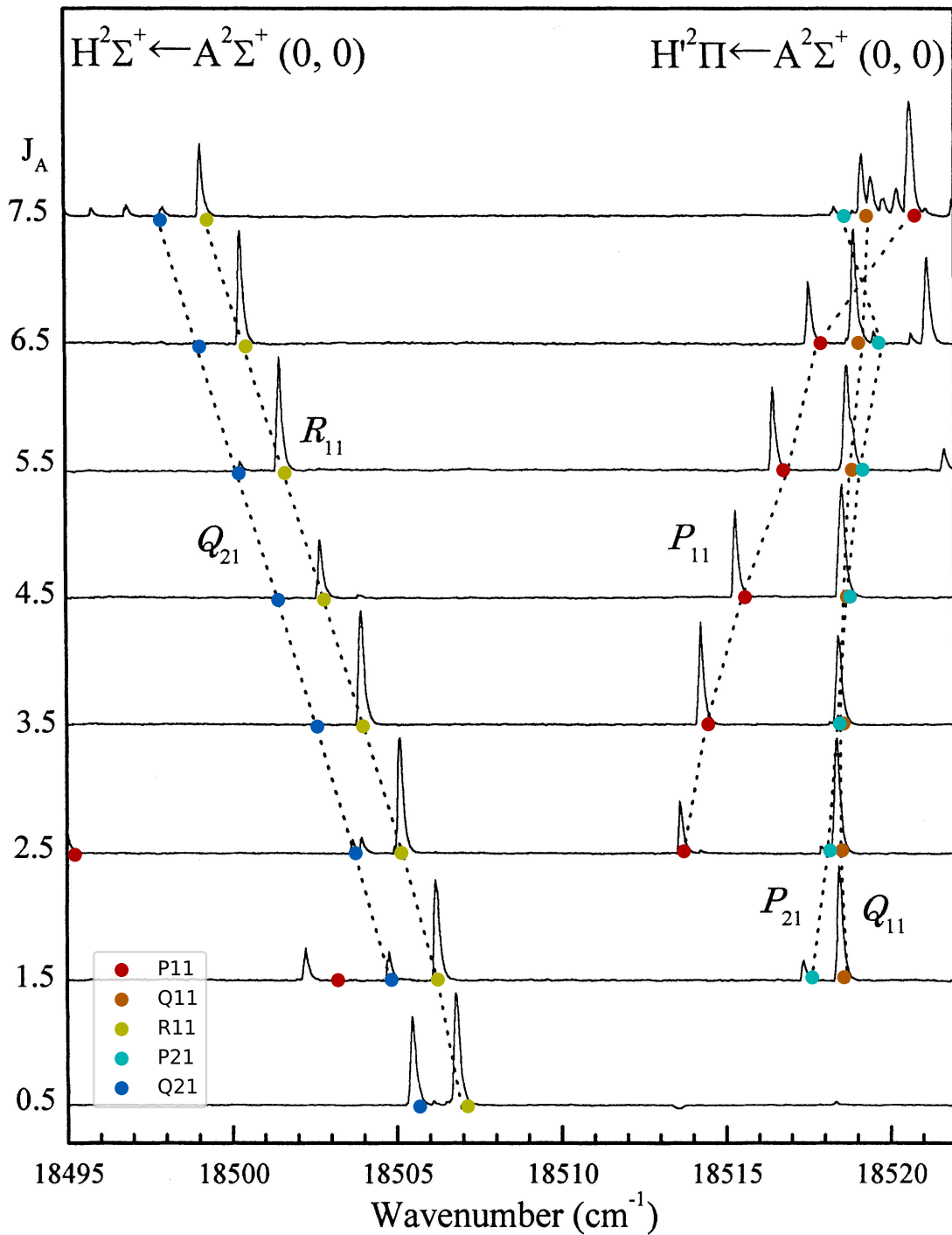


Figure 12: The background figure is taken from [3]. The transitions were measured using a C500 dye laser with a wavelength of about 540 nm. The color coded circles are the result of the simulation presented above, where only X_{Y1} transitions are shown. The simulation data matches closely in most cases with the data from [3] and their theoretical prediction, illustrated by dashed lines.

5 Experimental Results

This chapter covers the measurements made, using the predicted transition locations from above. All measurements were made at a pressure of 0.7 mbar nitric oxide in the cell. The voltage across the cell was set to 10 V. Since there was only little nitric oxide loss due to decomposition and other factors to be expected, the gas apparatus, including all the pipes leading to and from the gas cell, was filled with nitric oxide once and all measurements on a given day were made with that filling. The measurements were conducted using the $A^2\Sigma^+ \leftarrow X^2\Pi$, $P_{12}(J_X = J_A + 1)$ transition for pumping the $A^2\Sigma^+$ state. J_Y describes the rotational quantum number J associated with the state Y for a transition involving states Y and Z . The $A^2\Sigma^+ \leftarrow X^2\Pi$, P_{12} transition was used, since the P_{12} branch is not overlapped by any other branch, which ensures that the correct transition is driven.

5.1 R_{11} transitions

First the measurement of the $H^2\Sigma^+ \leftarrow A^2\Sigma^+$, $R_{11}(J = 4.5)$, that had been measured in [20] with the same measurement setup, was repeated. The electronic signal produced by the strong transition is clearly visible in 13, after filtering the high amounts of electronically induced noise, due to long, unshielded wires between the gas cell and the preamplifier, of 50 Hz and higher. This measurement was only to confirm, that the measurement apparatus still worked as intended. Thus no additional data, like green power drifts over the frequency sweeps and cavity signals, was recorded. For more information on the transition see [20].

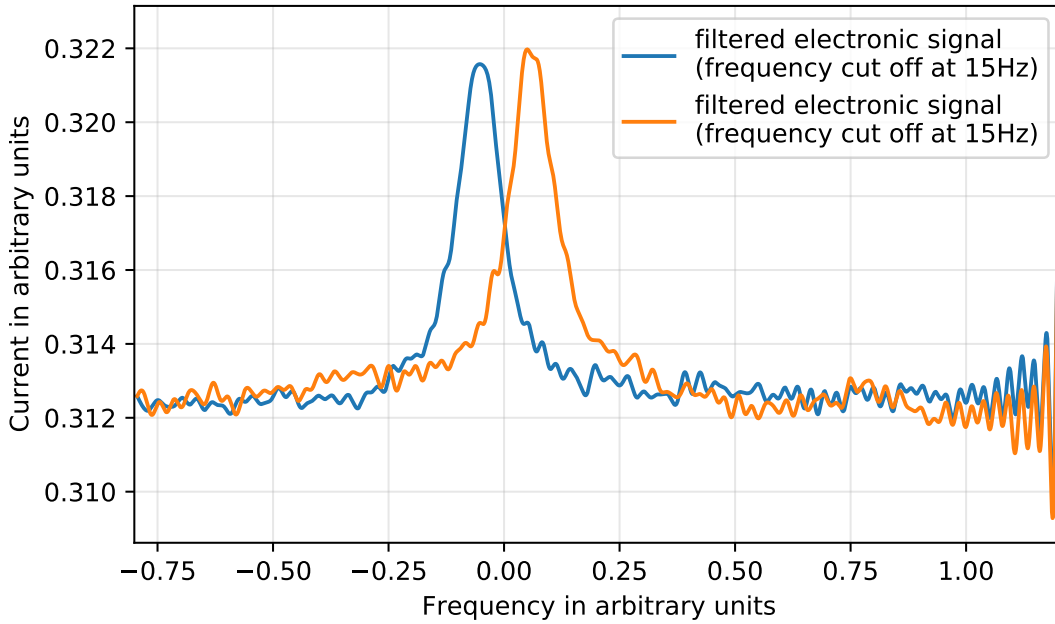


Figure 13: $H^2\Sigma^+ \leftarrow A^2\Sigma^+$, $R_{11}(4.5)$. The blue line represents a sweep with decreasing frequency detuning, the orange line represents a sweep with increasing frequency detuning. The transition gives a change of 9 pA in the electronic signal. The transition was only visible using a cutoff in frequency space with $f_0 < 45$ Hz. The features on the right are an artifact due to the frequency cutoff in measurement data while filtering in Fourier space.

The second transition measured of the R_{11} branch was $\text{H}^2\Sigma^+ \leftarrow \text{A}^2\Sigma^+$, $R_{11}(J = 0.5)$. The transition was visible in the noise on the oscilloscope, without filtering the data. Still, the signal was filtered with a cutoff in frequency space with $f_0 = 5$ Hz. The resulting electric signal is shown in figure 14. The peak from the sweep with increasing frequency detuning is shifted to higher frequencies, since the molecules need time to reach the electrode. The sweep with decreasing frequency detuning shows opposite behavior. The FWHM of the peak is ~ 475 MHz.

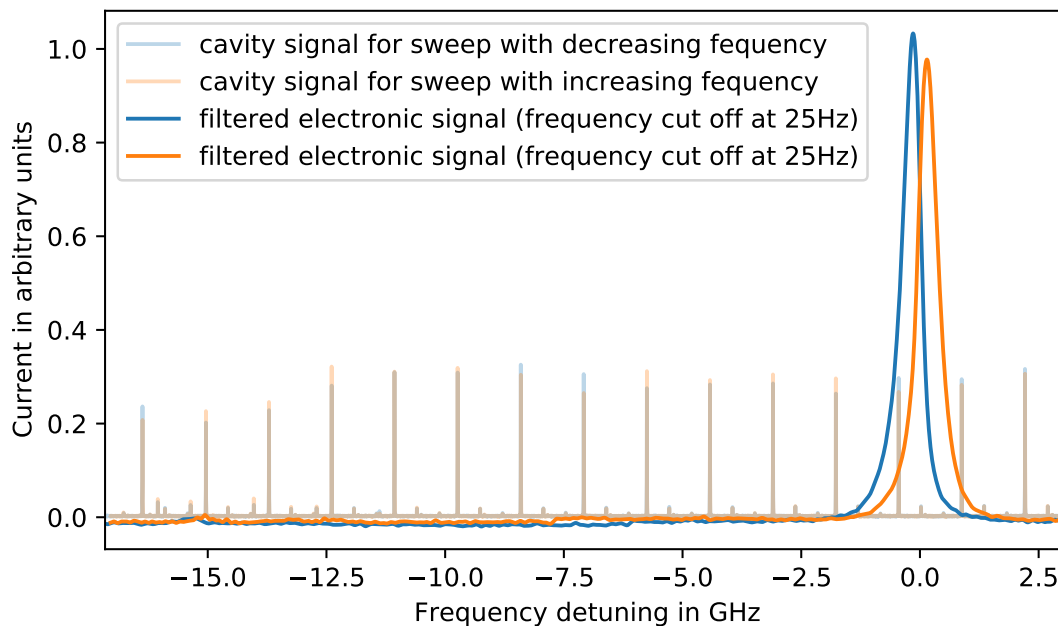


Figure 14: $\text{H}^2\Sigma^+ \leftarrow \text{A}^2\Sigma^+$, $R_{11}(0.5)$. Blue lines represent a sweep with decreasing frequency detuning, orange lines represent a sweep with increasing frequency detuning. For detuning below -12 GHz the laser shows signs of mode hops, which can be recognized by the decrease in amplitude and irregularity of side modes of the cavity signal.

5.2 $\text{H } ^2\Sigma^+ \leftarrow \text{A } ^2\Sigma_{F_1}^+, J_A = 1.5$

After improving the cabling from the gas cell to the preamplifier by exchanging the two wires with a BNC cable, the noise was reduced significantly to a level where no additional filtering was required. The triplet of transitions from $\text{A } ^2\Sigma_{F_1}^+$ to $\text{H } ^2\Sigma^+$ with $J_A = 1.5$ was measured. R_{11} and P_{11} were found where they were shown in [3] and where the simulation put them within 30 GHz in case of the P_{11} transition and below for other transitions. The double feature labeled as Q_{21} needs further evaluation which was not possible in the time frame of this thesis. Reasons for the existence of these two features could be caused by unidentified mode hops or inaccuracy of the wavemeter, thus further investigation is required. The R_{22} transition was not found as was expected due to $\text{A } ^2\Sigma^+$ being driven to F_1 starting from $\text{X } ^2\Pi_{F_2}$ using a P_{21} transition. All measured data is shown in 15.

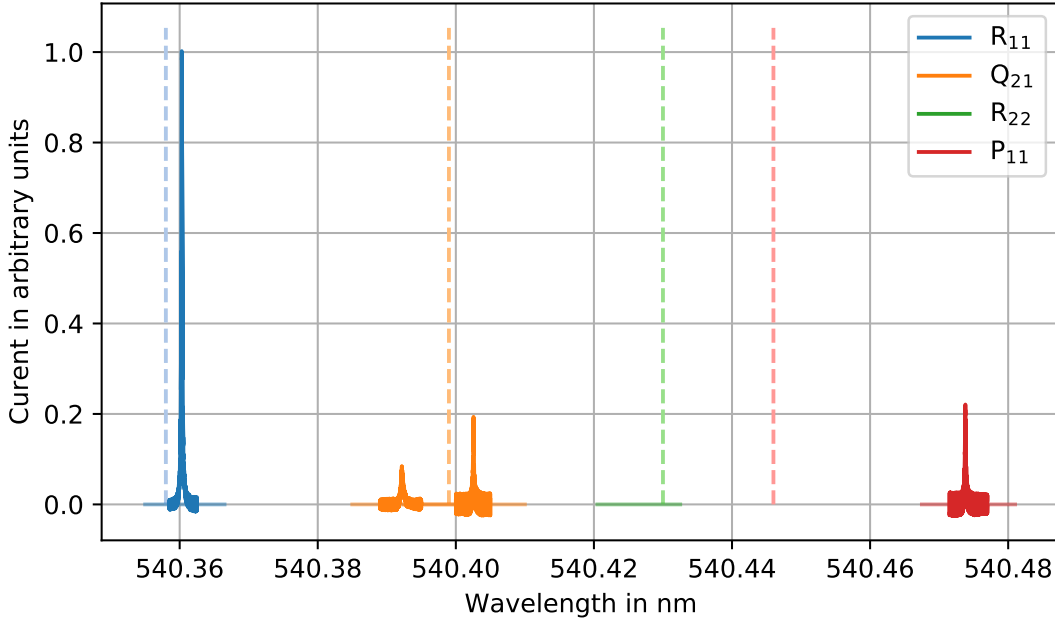


Figure 15: All possible $\text{H } ^2\Sigma^+ \leftarrow \text{A } ^2\Sigma_{F_1}^+, J_A = 1.5$ transitions. R_{22} was confirmed as not driveable from $\text{A } ^2\Sigma_{F_1}^+$. As can be seen in figure 12, the matching of the P_{11} transition is off by ~ 30 GHz, while the other transitions match up within 5 GHz.

The R_{11} transition in figure 15 is viewed separately, as shown in figure 16. The curve can be described by a Lorentzian function of the form

$$f(x) = \frac{a}{\pi \cdot \gamma \left(1 + \left(\frac{x-x_0}{\gamma} \right)^2 \right)} \quad (29)$$

with an amplitude a , HWHM γ and positional shift x_0 . The fit parameters found are listed in table 4. A very nearly realized Lorentzian function is expected as the feature profile, since the lower transition $A^2\Sigma^+ \leftarrow X^2\Pi$ is driven with a locked laser of a relatively narrow width of < 200 MHz versus the Doppler shift induced transition line width of 3 GHz, which selects only a narrow velocity distribution and drives them to the corresponding $A^2\Sigma^+$ state from which the next transition is driven. The FWHM of this transition is thus $f_{\text{FWHM}} = 127.2$ MHz.

fit parameter	dec. freq.	inc. freq.
a in a. u.	0.2045	0.2004
γ in GHz	0.0644	0.0628
x_0 in GHz	-0.0154	0.0117

Table 4: This table lists the fit parameters found for the Lorentzian function (see equation 29) describing the transitional peak of the $H^2\Sigma^+ \leftarrow A^2\Sigma^+$, R_{11} transition. “dec. freq.” stands for a sweep with decreasing frequency, “inc. freq.” stands for a sweep with increasing frequency.

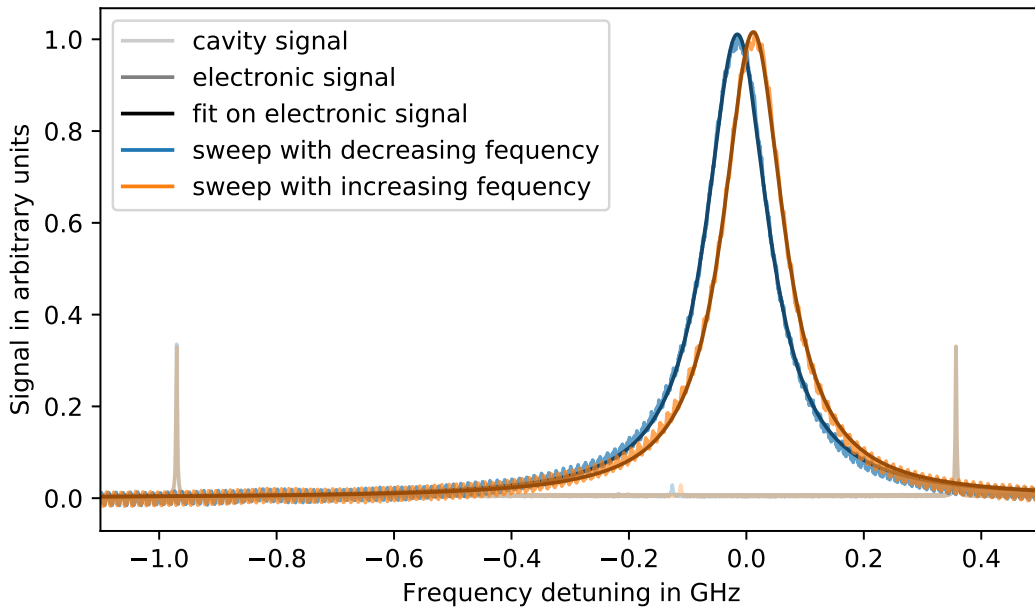


Figure 16: $H^2\Sigma^+ \leftarrow A^2\Sigma^+$, R_{11} , $J_A = 1.5$ transition. A Lorentzian function is fitted to the data. Fit parameters are listed in table 4. The fit, shown by a dark line, black in legend, is plotted on top of the data, shown by lighter line in plot. The very light lines show the cavity signal.

5.3 Measurement stability

5.3.1 1080 nm long term frequency stability

The drift in frequency of the 540 nm laser was a concern, since averaging over large times with a drifting laser, due to temperature, air pressure, etc., could lead to a massive broadening of the desired peak. To gauge the magnitude of the frequency drift, a cavity signal was recorded. One peak was selected and tracked over time. Resulting from the relative shift of the peak in relation to the distance between two peaks with a frequency distance of $f_{\text{FSR}, 780 \text{ nm}} = 918.8 \text{ MHz}$, figure 17 was produced. Over $\sim 20 \text{ min}$ the laser drifted by 25 MHz. With a FWHM of $\sim 500 \text{ MHz}$, the frequency drift is with $\sim 5\%$ of a typical FWHM negligible. Due to this finding, all measurements above were taken by averaging the data from the preamplifier directly in the oscilloscope.

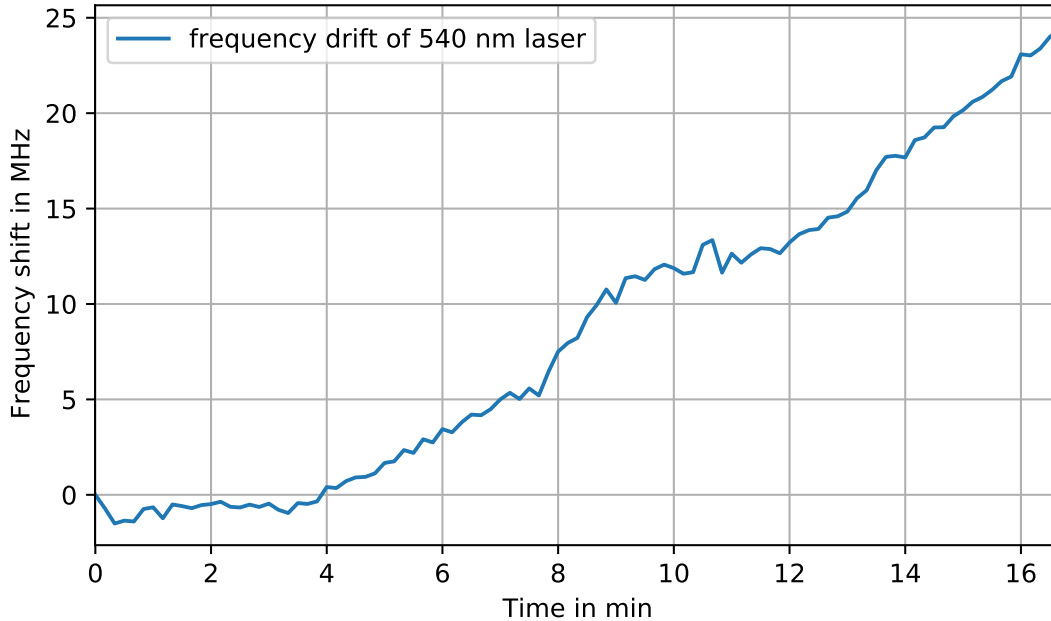


Figure 17: Frequency drift of the 540 nm laser. Drift has been calculated by recording cavity peaks of a stabilized cavity produced by the 540 nm laser. Peak shifts are scaled according to the known $f_{\text{FSR}, 780 \text{ nm}} = 918.8 \text{ MHz}$.

5.3.2 Mode hops

When mode hops occur, the laser changes its wavelength suddenly, which may lead to the appearance of spectroscopy lines at unexpected positions, due to an arbitrary transition driven by chance. Since the duration of the laser at the required frequency to drive the transition is random, the amount of driven molecules varies and thus the current produced by the transition which happens by chance. In comparison to that, transitions driven with a stable laser frequency are more reliably driven and thus the current produced is almost constant over multiple sweeps, only varying with the power output of the laser. This correlation is easily seen in figure 18.

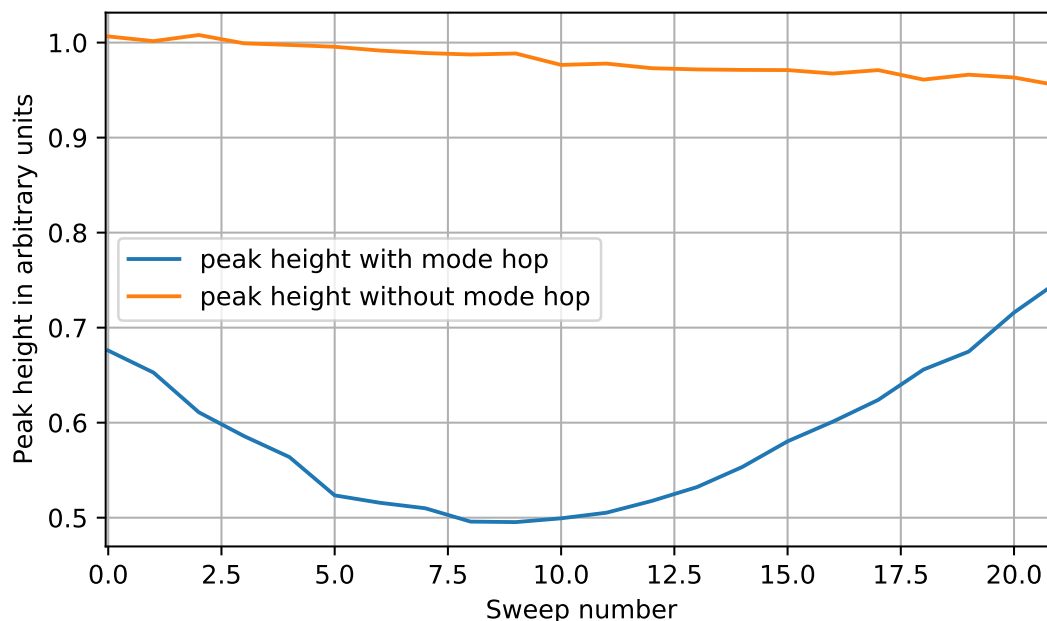


Figure 18: Peak height with and without mode hop. The peak height for driven transition without mode hop is nearly constant, while the transition driven with mode hop varies widely. Both lines were taken from the same measurement cycle. The variation in current produced by the mode hop cannot be produced by laser power fluctuations, since the power was monitored and from sweep to sweep almost identical.

5.3.3 Line strength

The line strengths of the recorded electric signal are not representative for several reasons. First, the gas setup is not operated in through flow but with a stationary gas filling. Due to possible small leaks and decomposition by the UV laser, the gas composition can change during measurements. Furthermore, the UV laser cannot be locked repeatedly on the exact same frequency. Since the UV laser is not locked centered on the absorption dip, small changes can have a large impact on the driving efficiency of the $A^2\Sigma^+ \leftarrow X^2\Pi$ transition. Additionally the 540 nm laser has a large power drift during scanning due to changes in phase matching between the incoming wavefront and the doubler crystal, as can be seen in figure 19. All of these factors make it difficult to make quantitative statements on the relative strength of different transition and need to be further improved upon.

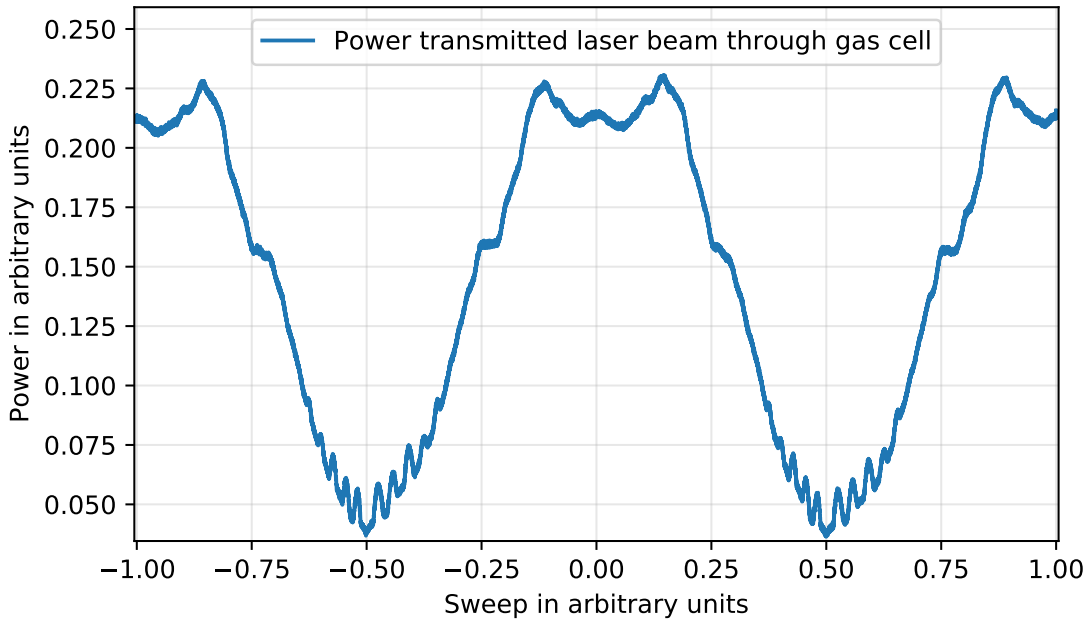


Figure 19: Green power drift over 2 sweeps. One sweep contains a sweep from the upper wavelength limit to the lower wavelength limit of the set scan range and back. The change in power is about five fold.

6 Summary and outlook

The requirement for a complete simulation of the $H^2\Sigma^+$, $H'^2\Pi$ states was motivated with the underlying goal of a trace gas sensor for nitric oxide using Rydberg excitation via a three photon transition scheme. The simulation was done using the basic energy levels calculated with the program pgopher with rotational constants taken from [2] and [17], while the necessary perturbations were done with a self-developed program. The perturbation parameters for the energy levels of the $H^2\Sigma^+$, $H'^2\Pi$ states were found using transitional data from [2]. After converting them to energy levels, the basic energy level simulation from pgopher was fitted using the A class perturbation theory presented in [1]. This is caused by rotational coupling between different electronic states of equal parity and sign regarding a reflection through an arbitrary plane containing the intermolecular axis. From the resulting energy level simulation of the $H^2\Sigma^+$, $H'^2\Pi$ states the $H^2\Sigma^+$, $H'^2\Pi \leftarrow A^2\Sigma^+$ transitions were calculated, which represent the experimental data quite well, as shown in figure 12. Additionally own data regarding the line width of $H^2\Sigma^+$, $H'^2\Pi \leftarrow A^2\Sigma^+$ transitions and the position of measured features in comparison to the simulated transitions was evaluated, to judge the quality of measurements achievable with the current setup.

Laser stabilization of the two used lasers was implemented in the course of the experimental part of this thesis. Problems regarding the goal of finding the strongest transition possible to drive the Rydberg excitation as efficiently as possible are still present. The experiment parameters need to be further improved to reach the above stated goal of efficient Rydberg excitation. These include power stabilization of the lasers involved in the measurement process and more fidelity in pressure regulation. When measurements are comparable and repeatable, the last Rydberg transitions can be further analyzed, which are used to excite the electrons into high Rydberg states, which can easily lead to ionization by collisions with other gas molecules. When the best transitions are found, the process of introducing background gases at different concentrations can start, which will eventually lead to a nitric oxide trace gas sensor for low volumina in gas samples.

References

- [1] G. Dieke. “A Class of Perturbations of Molecular Levels”. In: *Physical Review* 47 (1935), pp. 870–876.
- [2] K.P. Huber et al. “Absorption spectrum of the NO molecule”. In: *Helvetica Physica Acta* 36 (1963), pp. 257–268.
- [3] Y. Ogi et al. “Laser-induced amplified spontaneous emission from the 3d and *nf* Rydberg states of NO”. In: *Chemical Physics* 255 (2000), pp. 379–395.
- [4] J. V. Zawadzki R. F. Furchgott. “The obligatory role of endothelial cells in the relaxation of arterial smooth muscle by acetylcholine”. In: *Nature* 288 (1980), pp. 373–376.
- [5] G. M. Buga L. J. Ignarro. “Endothelium-derived relaxing factor produced and released from artery and vein is nitric oxide”. In: *PNAS* 84 (1987), pp. 9265–9269.
- [6] E. A. Higgs S. Moncada. “The discovery of nitric oxide and its role in vascular biology”. In: *British Journal of Pharmacology* 147 (2006), pp. 193–201.
- [7] L. Ridnour D. Thomas. “The chemical biology of nitric oxide: Implications in cellular signaling”. In: *Free Radical Biology and Medicine* 45 (2008), pp. 18–31.
- [8] H. Ischiropoulos. “Biological Tyrosine Nitration: A Pathophysiological Function of Nitric Oxide and Reactive Oxygen Species”. In: *Archives of Biochemistry and Biophysics* 356 (1998), pp. 1–11.
- [9] S. Asai D. Bellin. “Nitric Oxide as a Mediator for Defense Responses”. In: *APS Publications* 26 (2013), pp. 271–277.
- [10] J. Schmidt M. Fiedler. “Proof of concept for an optogalvanic gas sensor for NO based on Rydberg excitations”. In: *Appl. Phys. Lett.* 113 (2018).
- [11] Fabian Munkes. “Continuous-wave absorption spectroscopy on the X 2Pi_{1/2} to A 2Sigma⁺ transition of nitric oxide”. Master thesis. 2019.
- [12] Gerhard Herzberg. *Molecular spectra and molecular structure*. Vol. 1. Spectra of diatomic molecules. Second edition, eighth printing. 1950. Chap. 3-4.
- [13] R. Oppenheimer M. Born. “On the Quantum Theory of Molecules”. In: *Annalen der Physik* 84 (1927), pp. 457–484.
- [14] S. Galembek R. Orena. “Molecular Orbitals of NO, NO⁺, and NO⁻: A Computational QuantumChemistry Experiment”. In: *J. Chem. Educ.* 91 (2014), pp. 1064–1069.
- [15] Joshua Fabian. “Design of an electrically contacted through-flow cell for ionization current detection of Rydberg states in nitric oxide”. Bachelor thesis. 2020.
- [16] Andre Bisquerra. “Setup and Characterisation of aFrequency-Doubled Lasersystemfor Spectroscopy of the A2Sigma⁺toH2Sigma⁺ Transition in Nitric Oxide”. Bachelor thesis. 2019.
- [17] C. Effantin A. Bernard. “On the 3d Rydberg states of the NO molecule”. In: *Molecular Physics* 73 (1991), pp. 221–234.

References

- [18] C. Western. “PGOPHER: A program for simulating rotational, vibrational and electronic spectra”. In: *Journal of Quantitative Spectroscopy and Radiative Transfer* 186 (2017), pp. 221–242.
- [19] *Nitric oxide*. URL: <https://webbook.nist.gov/cgi/cbook.cgi?ID=C10102439&Mask=1000#Diatomic> (visited on 10/02/2020).
- [20] Yannick Schellander. “Ionization current measurements of Rydberg states in nitric oxide created by continuous-wave three-photon excitation”. Master thesis. 2020.

Danksagung

Mein Dank gilt Prof. Dr. Tilman Pfau für die Möglichkeit, die Bachelorarbeit am 5. physikalischen Institut schreiben zu dürfen.

Weiterer Dank gilt an Dr. Harald Kübler für die Vergabe der Bachelorarbeit an seiner Arbeitsgruppe.

Dank gilt auch Patrick Kaspar für seine Betreuung meiner Bachelorarbeit.

Zusätzlich möchte ich Fabian Munkes und Benjamin Renz für das Probe lesen einzelner Kapitel danken.

Abschließend möchte meinen Eltern danken, die mir das Studium ermöglicht haben und mir während des gesamten Studiums den Rücken frei gehalten haben.